

Matching entropy based disparity estimation from light field

LIGEN SHI,¹ CHANG LIU,² DI HE,² XING ZHAO,^{1,*} AND JUN QIU^{2,*}

¹*School of Mathematical Science, Capital Normal University, Beijing 100048, China*

²*Institute of Applied Mathematics, Beijing Information Science and Technology University, Beijing 100101, China*

**zhaoxing_1999@126.com*

**qiu.jun.cn@ieee.org*

Abstract: A major challenge for matching-based depth estimation is to prevent mismatches in occlusion and smooth regions. An effective matching window satisfying three characteristics: texture richness, disparity consistency and anti-occlusion should be able to prevent mismatches to some extent. According to these characteristics, we propose matching entropy in the spatial domain of light field to measure the amount of correct information in a matching window, which provides the criterion for matching window selection. Based on matching entropy regularization, we establish an optimization model for depth estimation with a matching cost fidelity term. To find the optimum, we propose a two-step adaptive matching algorithm. First, the region type is adaptively determined to identify occluding, occluded, smooth and textured regions. Then, the matching entropy criterion is used to adaptively select the size and shape of matching windows, as well as the visible viewpoints. The two-step process can reduce mismatches and redundant calculations by selecting effective matching windows. The experimental results on synthetic and real data show that the proposed method can effectively improve the accuracy of depth estimation in occlusion and smooth regions and has strong robustness for different noise levels. Therefore, high-precision depth estimation from 4D light field data is achieved.

1. Introduction

Light fields [1, 2] record the spatial and angular information of sets of light rays in scene space and have been widely used in scene depth estimation and 3D estimation [3, 4]. Adelson et al. [5] proposed the 7D plenoptic function $L(V_x, V_y, V_z, \phi, \varphi, \lambda, t)$ to describe the irradiance information of a light ray with any wavelength in space at any time. Then, a 4D light field, which is a simplified two-plane representation suitable for optical imaging systems, was developed [6]. There are four categories of methods used to estimate depth information from a 4D light field: matching-based, epipolar geometry-based, focus measure-based and deep learning-based methods. Matching-based methods [7–13] are an extension of the stereo matching method, which can reduce the influence of light field spectrum aliasing and angular artifacts. However, matching often fails in smooth and occlusion regions. Epipolar plane images (EPIs) reveal the epipolar geometry of light fields [14–17]. Therefore, the depth can be obtained by calculating the slope of the epipolar line in an EPI. Epipolar geometry-based methods can achieve good results in occluded regions, but they require a large amount of calculation and are sensitive to noise. Focus measure-based methods obtain the depth by the focus measure in the focal stack [18–21]. Since the focal stack is the projection of the light field in the preset depth layers, the estimation accuracy depends on sampling of layers. Deep learning-based methods replace complex depth estimation pipelines with neural networks [22–25], which require a large amount of training data and lack generalization abilities.

Area matching is a commonly used technique in matching-based methods and makes use of window matching instead of pixel matching to improve the robustness. A unified matching

window leads to calculation redundancy in textured region and mismatches in occluded and smooth regions. If we can determine the occluding, occluded, smooth and textured regions, we will be able to improve the estimation accuracy and efficiency by selecting the effective window size and shape for different regions. For textured and smooth regions, selecting a matching window that covers enough textures is the key task. For occluding regions, selecting the shapes according to the occlusion geometry is the key task. For occluded regions, selecting the shape of the matching windows and the visible viewpoints are the key tasks.

To accomplish the key tasks, an effective matching window should satisfy three characteristics: texture richness, disparity consistency and anti-occlusion, thus will provide enough valid matching information and less invalid or incorrect information. We propose matching entropy corresponding to these characteristics to measure the effectiveness of a matching window. With matching entropy acting as the regularization term, we establish an optimization model for depth estimation and propose a two-step adaptive window matching method to solve the optimization model. In the first step, the region type is adaptively determined based on segmentation and texture information. In the second step, matching entropy is used as a criterion for the adaptive selection of the matching windows' shape and size, and the visible viewpoints.

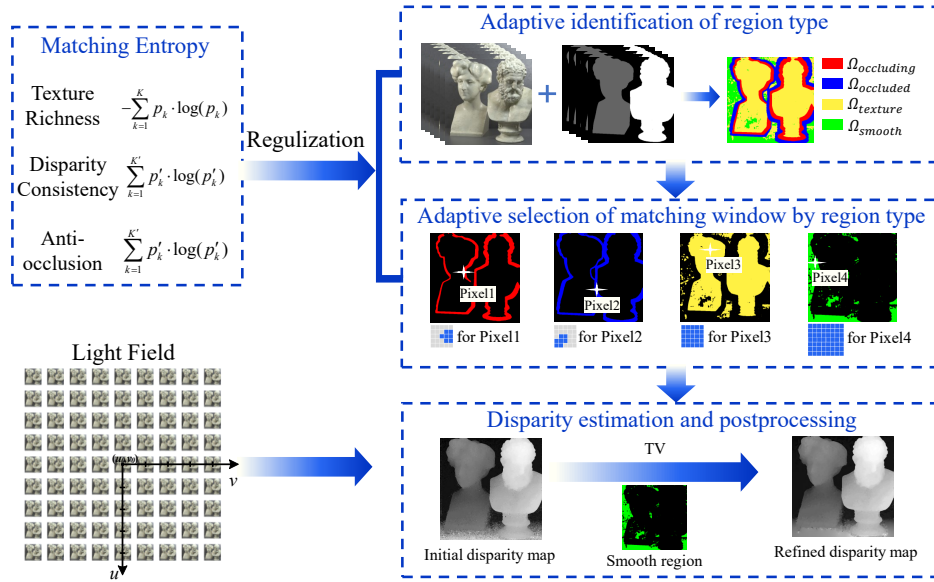


Fig. 1. Scheme of the proposed matching entropy based disparity estimation. For the whole disparity estimation scheme, the fidelity term of the optimization model should be expressed here. The light field is also the beginning of the two steps.

2. Related work

Since sub-aperture images can be regarded as multiview images, the scene depth estimation approach that matches sub-aperture image arrays comes from area matching in stereo matching [26]. The designs of matching windows and the matching costs are the key problems of area matching. Typical matching windows include weighted windows [27], reliable multi-scale and multi-windows (MSMWs) [28], and cross-based local windows [29]. A weighted window is a fixed shape window with radiance- or distance-based weights for pixels. An MSMW is selected from a window dictionary by minimizing the matching cost. A cross-based window is generated

by expanding in a crisscross pattern according to the color consistency. The commonly used matching costs include the sum of absolute differences (SAD), the sum of squared differences (SSD), the normalized cross correlation (NCC), and census [30].

Sub-aperture images can be regarded as the dense uniform sampling on a viewpoint plane with a small baseline. The small baseline leads to subpixel disparities, which can hardly be detected using conventional matching methods. Spatial interpolation can be used to solve this problem to a certain extent. However, the blur caused by the interpolation increases the possibility of mismatches. Jeon et al. [8] proposed the phase shift theorem to allow the estimation of the subpixel offset between sub-aperture images. To reduce the mismatches in the occlusion region, Navarro J et al. [7] used an MSMW [28] to estimate the disparity between the central view and the rest of the views in the same row and column and then used the median operator to extract the reliable disparity value. Chen C et al. [9] proposed a bilateral metric considering the color consistency and the pixel distance in the reference window to improve the robustness in occlusion regions, but this method is sensitive to noise. Williem W et al. [19] proposed the analysis of angular patches to form a matching cost by combining the angular entropy metric and adaptive defocus response. The angle entropy metric is more robust to occlusion but sensitive to noise. The balance between angle entropy and the adaptive defocus response is intractable. Wang T C et al. [20] proposed an occlusion-aware depth estimation method that can deal with occluded line edges. The accuracy of the depth estimation result is highly dependent on edge detection. Using occlusion-noise aware data costs, the constrained entropy cost in angular domain of light field is proposed to reduce the effects of the dominant occluder and noise in the angular patch, resulting in a low cost [31]. For super-resolution and disparity estimation, a generic mechanism to disentangle the coupled information for LF image processing, and a class of domain-specific convolutions is designed to disentangle LFs from different dimensions [32].

To reduce the mismatches in occluded and smooth regions, we propose matching entropy in the spatial domain of light field to measure how well a matching window in different regions meets the three characteristics. The optimization model based on matching entropy regularization is utilized for depth estimation in occlusion, smooth and textured regions.

3. The optimization model based on matching entropy regularization

The fixed window for area matching leads to mismatches in occlusion and smooth regions. It is an effective way to eliminate the pixels that cause mismatches and increase the amount of information used for correct matching. We proposed the matching entropy measure the correct information in a matching window, and hence, it becomes a criterion for the matching window design. With matching entropy acting as the regularization term, the depth estimation optimization model is established with an matching fidelity term.

3.1. Matching entropy

To estimate the depth map accurately, every matching window $w(x, y)$ needs to contain a sufficient amount of effective matching information. The ideal matching window should satisfy three characteristics: texture richness, disparity consistency and anti-occlusion. Texture richness is fundamental for area matching. Disparity consistency is the basic assumption of area matching, which ensures that the area remains invariant in different view images. Anti-occlusion is essential for accurate and robust matching in occlusion regions. According to these characteristics, we define the matching entropy of a window $w(x, y)$ to measure the amount of effective matching information.

Definition 1 For a light field $L(u, v, x, y)$, the matching entropy of a window $w(x, y)$ in the

central view image $L_{(u_0, v_0)}(x, y)$ is defined as

$$E^{entropy}[w(x, y)] = - \sum_{k=1}^K p_k \cdot \log(p_k) + \alpha_1 \sum_{k=1}^{K'} p'_k \cdot \log(p'_k) + \alpha_2 \sum_{k=1}^{K''} p''_k \cdot \log(p''_k), \quad (1)$$

where p_k and p'_k stand for the probabilities of the gray value and the disparity value of the k -th pixel in $w(x, y)$, respectively, while p''_k is the probability of the gray value of the k -th pixel of the mismatched pixels in $w(x, y)$. $\alpha_1 \geq 0$ and $\alpha_2 \geq 0$ denote the weight coefficients. $\alpha_2 = 0$ when there is no occlusion in $w(x, y)$.

The three terms of the matching entropy function refer to texture richness, disparity consistency and anti-occlusion. p_k and p'_k are calculated from the gray histogram and disparity histogram of $w(x, y)$, respectively, and p''_k is obtained from the gray histogram of the mismatched pixels in $w(x, y)$. In the anti-occlusion term, the mismatched pixels are the occluded pixels in $w(x, y)$ if Pixel (x, y) occludes other pixels, and they are the occluding pixels if Pixel (x, y) is occluded.

3.2. The optimization model

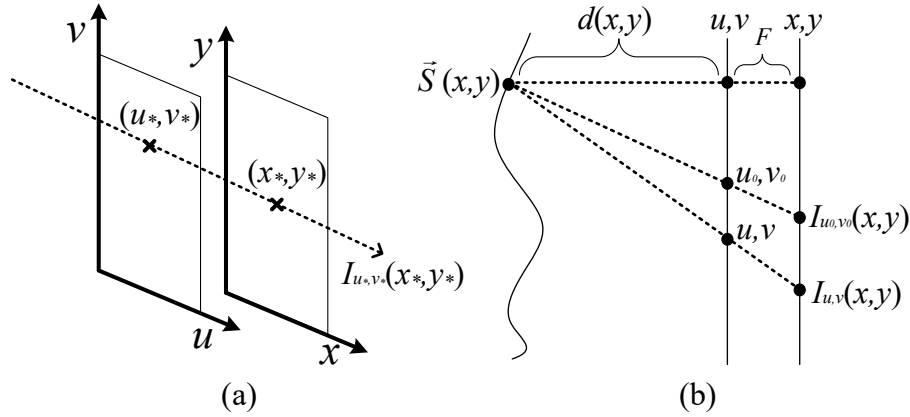


Fig. 2. (a) Two-plane parameterized light field. (b) Diagram of the scene point projected in different views. (u, v) and (x, y) represent the viewpoint plane and the image plane, respectively. F is the distance between the two parameterization planes, (u_0, v_0) is the central viewpoint, and $d(x, y)$ is the depth of the scene point $\vec{S}(x, y)$.

In the light field data, the scene point is projected in different views, as shown in Fig. 2. The relationship between the scene point $\vec{S}(x, y)$ and the depth map $d(x, y)$ is

$$\vec{S}(x, y) = \left(-\frac{Fx}{d(x, y)} + u_0, -\frac{Fy}{d(x, y)} + v_0, d(x, y) \right)^T. \quad (2)$$

The disparity of a scene point $\vec{S}(x, y)$ between adjacent viewpoint images is denoted as $disp(x, y)$. The relationship between $disp(x, y)$ and $\vec{S}(x, y)$ is

$$\vec{S}(x, y) = \left(-x(disp(x, y) - 1) + u_0, -y(disp(x, y) - 1) + v_0, \frac{F}{disp(x, y) - 1} \right)^T. \quad (3)$$

The coordinates of $\vec{S}(x, y)$ from viewpoint (u, v) are denoted as $(x, y)_{u, v}$. Then, the relationship between the image coordinates under viewpoints (u_0, v_0) and (u, v) is

$$(x, y)_{u, v} = (x, y)_{u_0, v_0} + ((u - u_0) \cdot disp(x, y), (v - v_0) \cdot disp(x, y)). \quad (4)$$

According to Eq. 4, we can define the matching term as the fidelity term of the optimization model as follows:

$$\begin{aligned} & E^{\text{match}}[disp(x, y), w(x, y)] \\ &= \sum_{(u, v) \in \Phi} \sum_{(m, n) \in w(x, y)} \beta_{(m, n)} \|L_{u_0, v_0}((x, y)_{u_0, v_0} + (m, n)) - L_{u, v}((x, y)_{u, v} + (m, n))\| \\ &= \sum_{(u, v) \in \Phi} \sum_{(m, n) \in w(x, y)} \beta_{(m, n)} \|L_{u_0, v_0}((x, y)_{u_0, v_0} + (m, n)) - L_{u, v}((x, y)_{u_0, v_0} \\ &\quad + ((u - u_0) \cdot disp(x, y), (v - v_0) \cdot disp(x, y)) + (m, n))\|, \end{aligned} \quad (5)$$

where Φ represents the set of visible viewpoints in the matching window $w(x, y)$, and $\beta_{(m, n)}$ is the weight coefficient.

Combining the matching entropy, we established the objective functional for disparity estimation.

$$E[disp(x, y), w(x, y)] = E^{\text{match}}[disp(x, y), w(x, y)] - \lambda E^{\text{entropy}}[w(x, y)], \quad (6)$$

where $E^{\text{entropy}}[w(x, y)]$ is the matching entropy term acting as the regularization term and λ is the regularization parameter.

By solving the following optimization problem, the disparity map can be estimated by selecting the effective matching windows in light of matching entropy.

$$[disp^*(x, y), w^*(x, y)] = \arg \min_{disp, w} (E(disp(x, y), w(x, y))). \quad (7)$$

Since the optimal matching windows contain sufficient effective information but no mismatching information, minimizing the fidelity term with the optimal windows by searching for disparities can realize accurate and robust estimation.

4. Implementation of depth estimation by adaptive region matching

4.1. Adaptive identification of region types

Since the selection of the matching window depends on the region type, the adaptive identification of the region type is the prerequisite for maximizing the matching entropy term.

4.1.1. Indicator for occluding and occluded regions

The central view image can be divided into occluding, occluded, textured, and smooth regions, which are labeled $\Omega_{\text{occluding}}$, Ω_{occluded} , Ω_{texture} and Ω_{smooth} , respectively. The region indicator function is denoted as $I(x, y)$.

$$I(x, y) = \begin{cases} 0, & (x, y) \in \Omega_{\text{occluding}} \\ 1, & (x, y) \in \Omega_{\text{occluded}} \\ 2, & (x, y) \in \Omega_{\text{texture}} \\ 3, & (x, y) \in \Omega_{\text{smooth}} \end{cases}. \quad (8)$$

A sub-aperture image array is a visualization of 4D light field data, as shown in Fig. 3. By varying the viewpoints, the occluding and occluded regions in the images will change. The

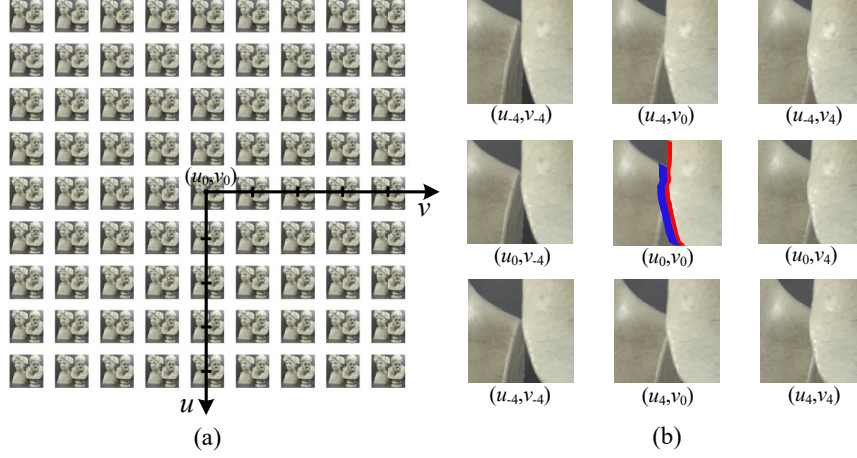


Fig. 3. (a) 9×9 sub-aperture images array of the Greek scene's light field. (b) The close-ups of sub-aperture images to Visually display occluding and occluded pixels.

occluding region is the edge area of the object that causes occlusion. Therefore, the light it emits is visible from all viewpoints. The occluded region is the edge area of the occluded object, and the light it emits is not visible from some viewpoints. Since occlusion only exists around the edges of objects, occluding and occluded regions can be identified by the differences between the segmentations of the central view image and other sub-aperture images. Considering the farthest sub-aperture images that are eight directions from the central view, the occluding and occluded regions can be determined by using the differences. Let $\tilde{\phi}$ be the viewpoint index set of the nine sub-aperture images used to indicate occlusion.

Applying alpha matting [33] to the sub-aperture images $L_{(u_i, v_j)}(x, y)$ and $(u_i, v_j) \in \tilde{\phi}$, we can obtain the segmentations $M_{(u_i, v_j)}(x, y)$, as shown in Fig. 4(b). According to the distance between the object and the lens plane, the object label in $M_{(u_i, v_j)}(x, y)$ is marked from large to small. The difference between the central view segmentation $M_{(u_0, v_0)}(x, y)$ and other segmentations $M_{(u_i, v_j)}(x, y)$ is calculated as

$$diff(x, y) = \sum_{(i, j) \in \tilde{\phi}} \left(M_{(u_0, v_0)}(x, y) - M_{(u_i, v_j)}(x + \Delta u, y + \Delta v) \right), \quad (9)$$

where $\Delta u = u_i - u_0$, $\Delta v = v_j - v_0$. Then, the occluded regions Ω_{occluded} and the occluding regions $\Omega_{\text{occluding}}$ can be identified.

$$\Omega_{\text{occluded}} = \{(x, y) \mid diff(x, y) < 0\}, \quad (10)$$

$$\Omega_{\text{occluding}} = \{(x, y) \mid diff(x, y) > 0\}. \quad (11)$$

4.1.2. Indicator for textured and smooth regions

In smooth regions, the intensities of pixels in a local neighborhood tend to be similar. Therefore, the statistical intensity characteristics in the neighborhood can be used to measure the smoothness, and then the smooth region Ω_{smooth} can be identified as

$$\Omega_{\text{smooth}} = \left\{ (x, y) \mid \psi(x, y) < \frac{N}{2}, (x, y) \notin \Omega_{\text{occluded}} \cup \Omega_{\text{occluding}} \right\}. \quad (12)$$

where N is the number of pixels in the local neighborhood of pixel (x, y) and $\psi(x, y)$ is the number of pixels within the neighborhood that have different pixel values from (x, y) .

After the occluding, occluded, and smooth regions are identified, the remaining regions are the textured regions Ω_{texture} . Taking the Greek scene and the Platonic scene as examples, the region identification results are shown in Fig. 4.

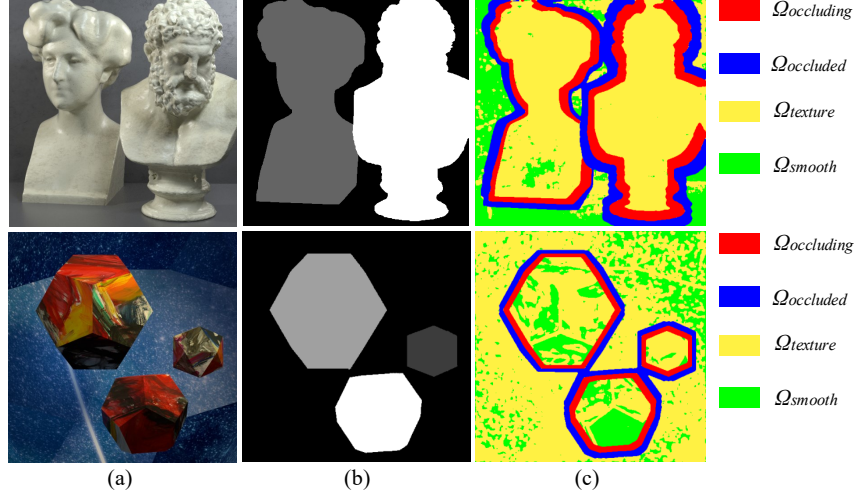


Fig. 4. Results of adaptive identifying the region types for Greek scene and Platonic scene. (a) The central view image. (b) The segmentation of the center view. (c) The region types. The occluding, occluded, texture and smooth regions are marked as the red pixels, the blue pixels, the white pixels and the black pixels respectively in (c).

4.2. Adaptive selection of matching window by region type

Based on the identified region, optimal matching windows can be designed for different regions. The shape and size of the windows are obtained by maximizing the matching entropy term. In this work, the disparity consistency part of the matching entropy term is calculated by the initial disparity map extracted from the images in the viewpoint set $\tilde{\phi}$.

4.2.1. Matching window selector and visible viewpoint set adoption for occlusion regions

For anti-occlusion in area matching, the matching window of occluding pixels should not contain occluded pixels, while the matching window of occluded pixels should not contain occluding pixels. As a result, the key for designing a matching window with high matching entropy is to find the effective shape of the matching window and the visible viewpoint set to exclude pixels in the opposite occlusion situation.

To design matching windows for occlusion regions, we should determine the shape and the size of each window. By considering the directions of the occlusion, we preset the eight window shapes, as shown in Fig. 5. We also preset the size range of the window from 3×3 to 15×15 . Then the optimal shape and size can be searched from the preset shapes and sizes to reach the maximum matching entropy.

Taking the occluded "Pixel1" in Fig. 6(a) as an example, Fig. 6(b) shows the relationship between the matching entropy values and the preset matching windows. The X-axis is the window shape labels, and the Y-axis is the matching entropy value. Different line colors represent different window sizes. For "Pixel1", the maximum matching entropy value is on the purple line,

whose X -axis is at 7, which means the optimal window should be a W_7 window with a size of 9×9 .

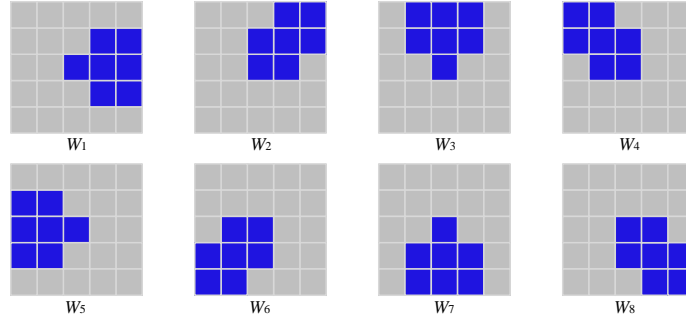


Fig. 5. The preset eight window shapes. The window shapes are marked as the green pixels.

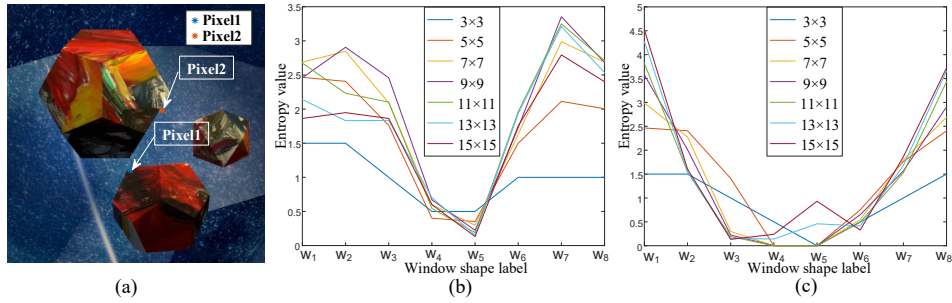


Fig. 6. (a) "Pixel1" and "Pixel2" are the representative pixels for the occluded pixel and the occluding pixel, respectively. (b) and (c) show the change curves of matching entropy as the window changes for "Pixel1" and "Pixel2", respectively. The colors of the curves represent windows of different sizes.

For smooth, textured and occluding regions, the windows are visible from all viewpoints; thus, ϕ in these regions should be a complete viewpoint set. For occluded regions, some pixels in the window are not visible from some viewpoints, so it is necessary to eliminate these viewpoints from the complete viewpoint set. According to the light field occlusion model [34], if the shape of the visible viewpoint set ϕ is consistent with the shape of the matching window, every pixel in the matching window is visible under the viewpoints in ϕ . For each window shape in $W_1 - W_8$ in Fig. 5, there is a corresponding visible viewpoint set in Fig. 7. For instance, the pixels in the matching window in Fig. 5 are visible under the viewpoints in Fig. 7(1).

To verify the effectiveness of the selection of the visible viewpoint set for occluded pixels, we calculate the matching cost of "Pixel2" in Fig. 6 under different disparity values with the traditional fixed matching window, adaptive matching window and adaptive matching window with the visible viewpoint set. The relationships between the disparity values and matching costs are denoted by the curves in Fig. 8. The ground truth is -1.42 , and the minimum point in (d) leads the most accurate disparity value.

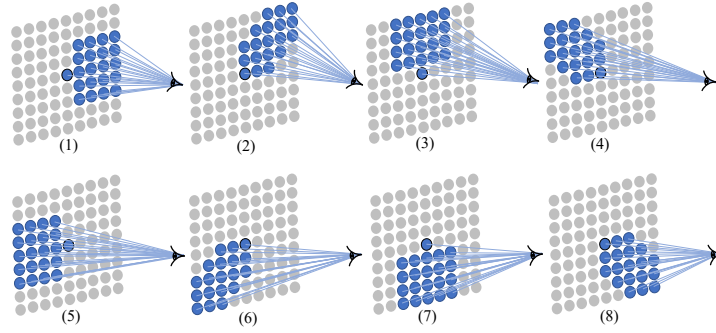


Fig. 7. Preset visual-viewpoint set. The blue viewpoint represents the visible viewpoint.

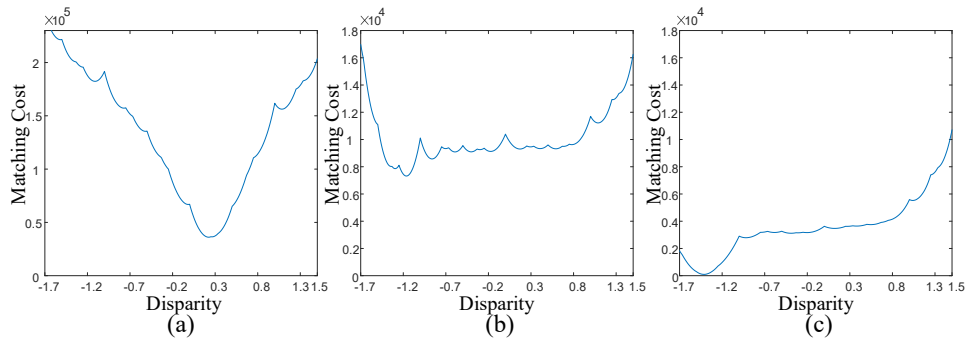


Fig. 8. The relationships between the matching costs and the disparity values via different matching windows and viewpoint sets. (a) The fixed square matching window with the complete viewpoint set. (b) The adaptively selected window with the complete viewpoint set. (c) The adaptively selected window with the visible viewpoint set.

4.2.2. Matching window selector for smooth and textured regions

In smooth and textured regions, the main consideration of the matching window design is to make the window size cover effective texture richness.

In Fig. 9, we select four pixels with different disparity consistencies from a neighborhood to verify the effectiveness of the designed matching window. The second row of Fig. 9 shows the relationship between the matching entropy value and the size of the matching window. The X -axis is the window size, and the Y -axis is the matching entropy value. "Pixel1" is the least consistent pixel, and "Pixel4" is the most consistent pixel. From the changing curve, the optimal window size for "Pixel1" is 3×3 , and the optimal window size for "Pixel4" is 11×11 .

4.3. Disparity estimation and postprocessing

4.3.1. Disparity estimation and refinement

After adaptively selecting the optimal matching window and determining the visible viewpoint sets, a disparity map can be estimated by minimizing the objective functional. Since the effective information of the matching windows in smooth region may be insufficient, the smooth region are shown as "black holes" in the disparity map. The total variation(TV) model [35] is used in the smooth region to eliminate the "black holes" and refine the disparity value $disp^*(x, y)$.

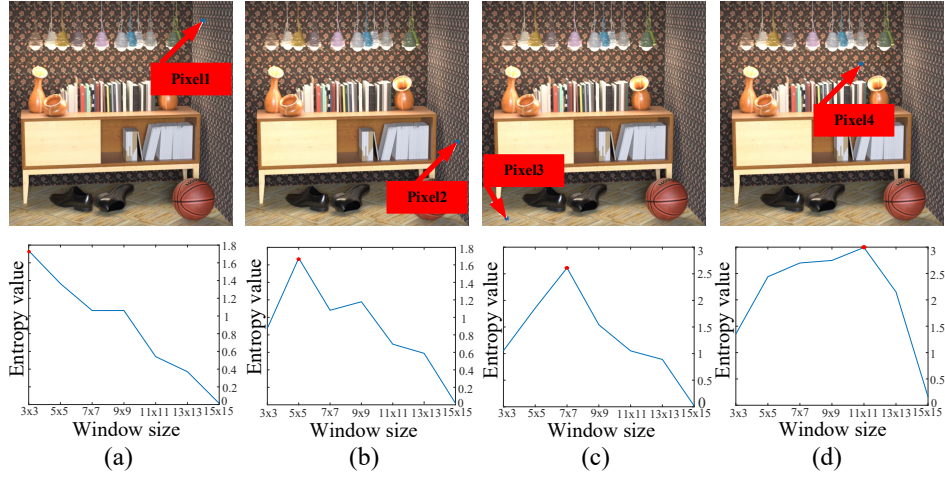


Fig. 9. Four typical matched pixels with different disparity consistencies, and the relationship between the matching entropy value and the window size. Adding enlarged images of the neighbourhood of Pixel1-Pixel4 to show the difference of the consistency.

$$\mu(x, y) = \arg \min_{\mu} \left\{ \iint_{\Omega_{\text{smooth}}} (\mu(x, y) - \text{disp}^*(x, y))^2 dx dy + \gamma |\nabla \mu(x, y)| dx dy \right\}. \quad (13)$$

where $\mu(x, y)$ is the disparity map refined by the TV model, $\nabla \mu(x, y)$ is the gradient of the disparity $\mu(x, y)$, and γ is the regularization parameter.

In addition, the line search method provides jagged estimation results. The TV model can reduce the jaggedness but blurs the edges at the same time. Therefore, we only apply TV in smooth regions.

5. Experimental results

In this section, experiments on both synthetic and real data are performed to evaluate the effectiveness of the proposed method. The standard light field data published in the 4D Light Field Benchmark Dataset [36] are used for the synthetic experiments, and we compare the result of our method with those of five other methods on the database. The real data are acquired by a camera with a three-axis translation platform.

5.1. Evaluation and comparison of the algorithms

In the 4D Light Field Benchmark dataset, the light field data provided for each scene are a 9×9 sub-aperture image arrays (with spatial resolutions of 512×512). We compared the performance of our method with that of the provided state-of-the-art methods: LF [8], epi1 [16], LF_OCC [20], MV [36], and mvcmv0 [36].

Four different scenarios are selected from the dataset to evaluate the performance of the proposed method, as shown in Fig. 10. The Backgammon scene is designed to assess the interplay of fine structures, occlusion boundaries and disparity differences. The Dots scene is designed to assess the effect of camera noise on the estimation of objects of varying sizes. The Pyramid scene is used to evaluate the performance of the algorithm in convex, concave, circular, and planar geometries. The Cotton scene is closer to a real scene with less artificial design and is used to evaluate the estimation accuracy in smooth and textured regions.

In Fig. 10, the disparity estimation results of the Backgammon scene show that LF_OCC and mvcmv0 produce noise at the edges, epi1 loses edge details, and LF produces a certain degree of blur at the gap between the jagged areas. In contrast, our method and MV can maintain the fine edge and gap structures. The results of the Dots scene show that our method is robust to noise. Our method, MV and epi1, can estimate more dot structures when the noise level is high. The results of the Pyramid scene show that our method and epi1 obtain smoother results on convex and concave inclined planes. For the Cotton scene, the estimation result of our method is blurred to a certain extent, but more details are maintained at the boundary of the foreground.

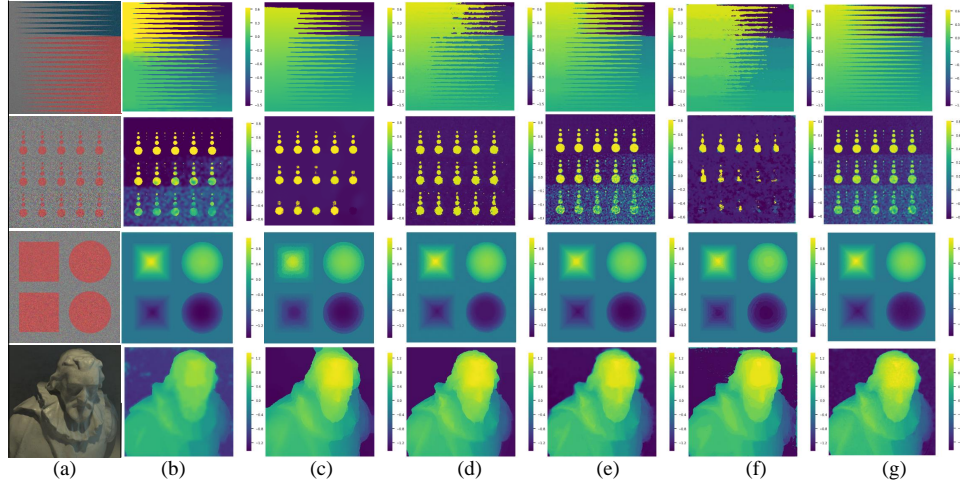


Fig. 10. Backgammon scene (1st row), Dots scene (2nd row), Pyramid scene (3rd row), and Cotton scene (4th row). (a) Central view image, (b) Our result, (c) LF, (d) LF_OCC, (e) MV, (f) mvcmv0, (g) epi1. The results of (c)-(g) come from [36].

We thoroughly assess and compare the six methods by summarizing all scores computed for each scene and the associated metrics into a radar chart. Each radar axis represents one metric, where the zero in the center represents perfect performance. Backgammon Thinning and Backgammon Fattening are used to evaluate the preservation of the fine structures in the Backgammon scenes. The Dots Missed Dots and the Dots Background mean square error (MSE) metrics are used to evaluate the anti-noise performance in the Dot scene. The Pyramids Bump Slanted and Pyramids Bump Parallel metrics are used to evaluate the smoothness of the slanted and parallel planes in the Pyramid scene. The MSE is the median MSE of the four scenarios and indicates the comprehensive performance of each method. The comprehensive performance of our method is at the middle level according to the MSE score. In terms of Pyramids Bump Slanted, Pyramids Bump Parallel, Dots Missed Dots and Backgammon Fattening, our method performs best. In terms of Backgammon Thinning, our method is mediocre. In terms of Dots Background MSE, the performance is weak. The overall performance indicates that our method can estimate more accurate disparity maps in smooth and textured regions and can handle occlusion regions well when the noise levels are high. Furthermore, with increases in the noise and fineness levels, the estimation accuracy of the background is more likely to decrease than that of the foreground structure.

5.2. Error analysis in occlusion regions

Occlusion exists at the edges of the scene, and the blurriness of the edges can reflect the estimation accuracy of the occlusion regions. To further evaluate the effectiveness of our method in occlusion

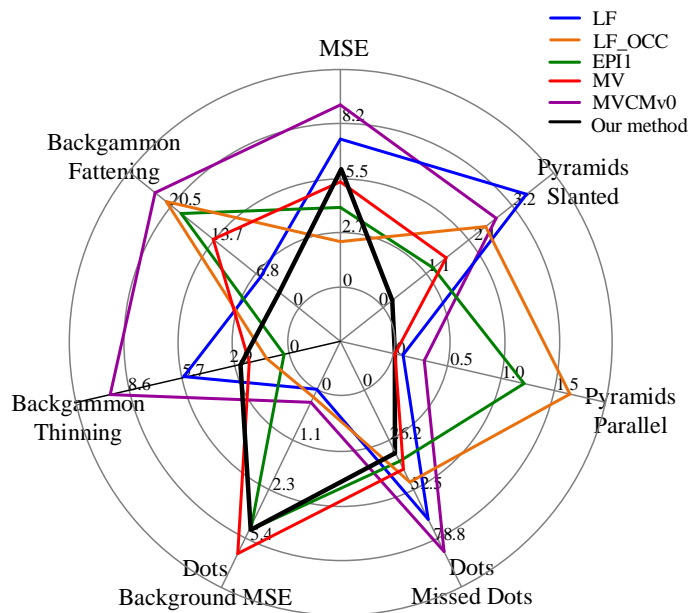


Fig. 11. The radar chart on the evaluation scenes. Our proposed matching entropy based method has advantages on several indicators.

and smooth regions, we analyze the Platonic scene in detail by drawing profiles to compare the ground truth disparity map and the calculated disparity map, as shown in Fig. 12. The profile positions are selected to include as many occlusion regions as possible, and we focus on the accuracy of the estimation results in the occlusion regions.

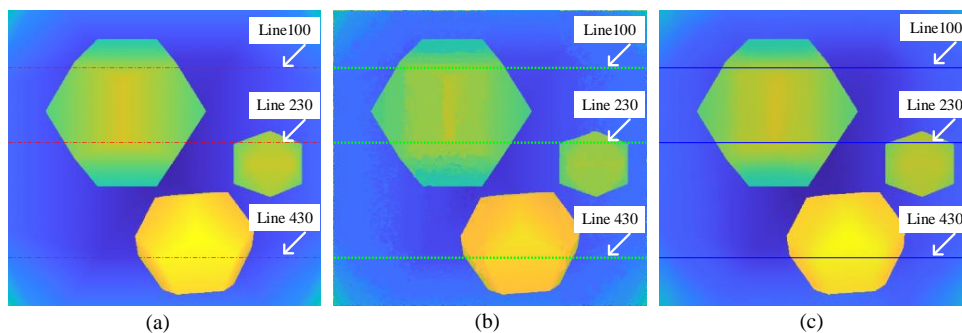


Fig. 12. The results of Platonic scene. (a) Ground truth of the disparity. (b) Initial disparity map. (c) Refined disparity map. And the positions of the profiles are marked, i.e., Line 100, Line 230 and Line 430.

Gaps in the disparity values will occur crossing object edges. In Fig. 13 (1) - (3), we notice that the initial disparity and the refined disparity values jump at the position where the ground truth disparity values jump. This shows that our method can maintain the edges well and can accurately estimate disparity values in occlusion areas. In addition, the profile is closer to the ground truth with fewer jagged areas and false jumps after TV refinement.

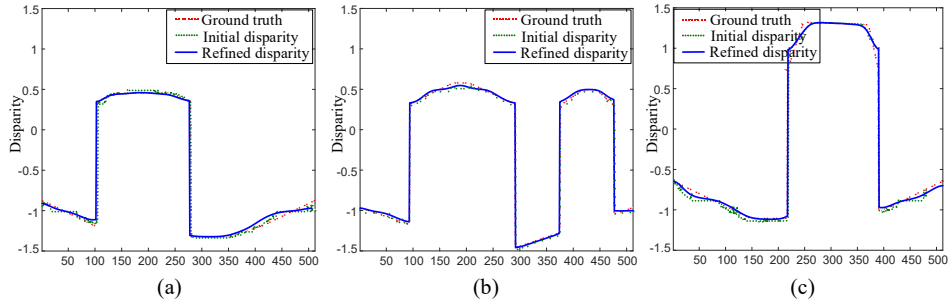


Fig. 13. Profiles of the disparity maps. (a) Profiles of Line 100. (b) Profiles of Line 230. (c) Profiles of Line 430. The red line represents the ground truth disparity, the green line represents the initial disparity, and the blue line represents the refined disparity.

5.3. Experiments on real data

In the experiment, a camera controlled by a three-axis translation platform is used to collect 2D images from 9×9 different viewpoints uniformly spaced in a plane at an interval of 0.5 mm to obtain 4D light field data. The resolution of the detector is 1280×980 , and the focal length of the lens is 35 mm.

The effectiveness of our method at the disparity gaps is verified in the first real data experiment, where four standard cubes are placed at four different depths in a range of [90, 100] cm. The effectiveness of our method when the depth changes continuously is verified in the second real data experiment, where regular-shaped blocks (standard pyramid, cuboid, cone, hemisphere, and cylinder) are placed in the depth range of [90, 100] cm. The effectiveness of our method and the benefit of refinement in smooth and occlusion regions in real scenario is verified in the third real data experiment, where a plant of tiger piran is placed at a depth range of [85, 100] cm.

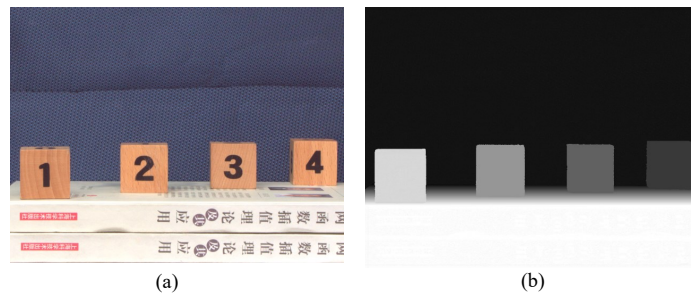


Fig. 14. The results of the second real data experiment. (a) Central view image of Cubes scene. (b) Disparity map.

Fig. 15(b) shows that the edges of every cube in the estimated disparity map are clear and sharp, which indicates that our method is able to handle depth gaps well. Fig. 14(b) shows that when the depth of the objects changes continuously, our method can maintain continuity in the estimation result.

Fig. 16 shows the result of the third real data experiment. We can see that our method can produce a disparity map with quite high accuracy for real scenes with smooth, textured and

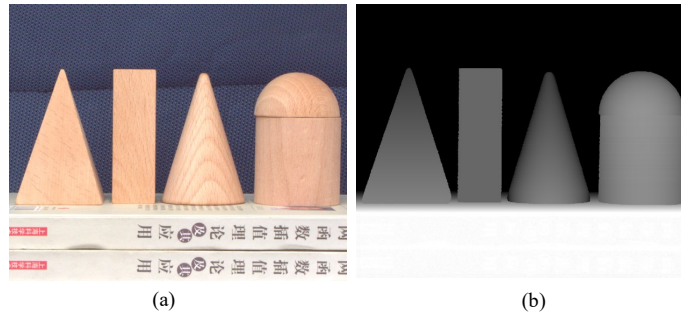


Fig. 15. The results of the first real data experiment. (a) Central view image of Regular-shaped Blocks scene. (b) Disparity map.

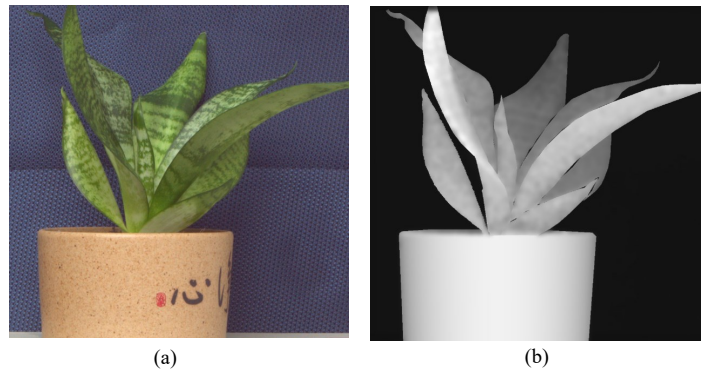


Fig. 16. The results of the third real data experiment. (a) Central view image of Tiger Piran scene. (b) Disparity map.

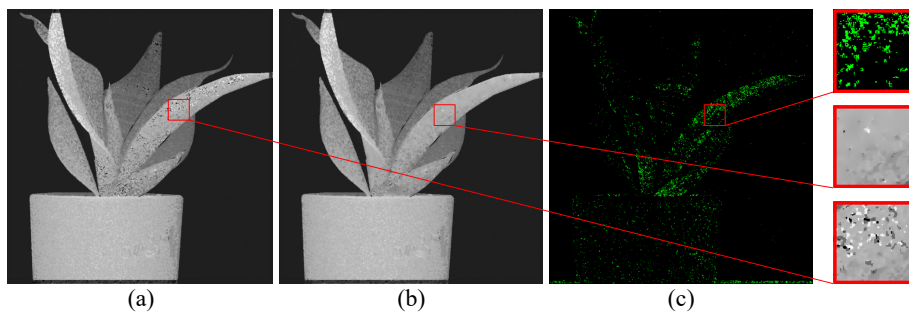


Fig. 17. Evaluations in the smooth regions. (a) Initial disparity map. (b) Refined disparity map by TV model. (c) Smooth region labeled map. The closed-ups are shown in the right column

occlusion regions. To further evaluate the benefit of TV refinement, we focus on the smooth and occlusion regions shown in Fig. 17 and Fig. 18. In Fig. 17, we notice that there are "black

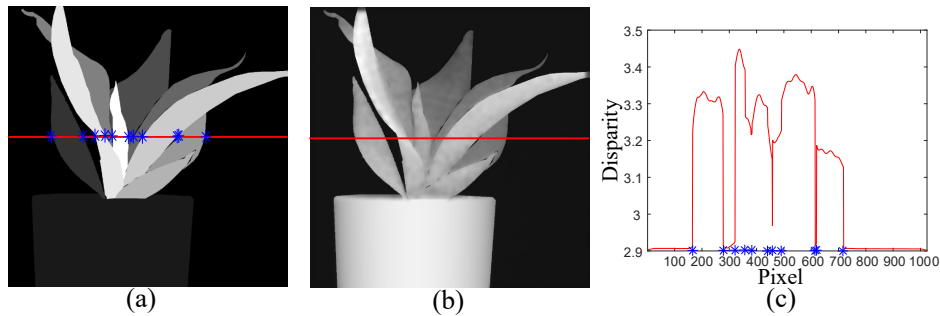


Fig. 18. Evaluations in the occlusion regions. (a) Segmentation of the central view image. (b) Disparity map estimated. (d) Profile and edge positions. The position of the profile is marked as the red line in (b) and (c), and the positions of the the edges where occlusion occurs are marked as blue star.

holes" in the initial disparity map due to the smoothness. The refinement can repair these "black holes" and improve the disparity estimation quality. In Fig. 18, we use the segmentation map to mark the edges where occlusion occurs. Then, we draw a profile (Line 480) and mark the edge positions on the profile as blue stars. Fig. 18(c) shows that the jumping positions of the profile coincide with the edge positions; that is, the refinement is able to preserve the edge information.

6. Discussion

sub-aperture image matching can be used to effectively estimate depth information only if matching windows contain sufficiently rich texture information, meet the consistency condition of the initial disparity, and retain only correct matching information when occlusion occurs. To measure the effectiveness of each matching window, the concept of matching entropy is proposed in this work to form the constraint for matching window selection and visible viewpoints set adoption. Considering the segmentation and the local correlation results, the region type identification function is constructed. Then, the optimal matching windows and the visible viewpoints in different regions are selected according to the matching entropy value. Finally, the objective functional can be minimized by the line search method, and the high-precision depth information can be estimated.

To verify the effectiveness of our methods, we conduct experiments with both synthetic and real light field data. For the synthetic experiments, we compare our methods with five other state-of-art depth estimation methods. From the experimental results, we conclude that our method can produce fairly accurate estimation results in scenes with different geometric structures and is robust to noise. When fine structures and occlusion exist in scenes, which often lead to severe mistakes for other depth estimation methods, our method performs quite well. The state-of-the-art disparity estimation results are obtained without using guided filtering and only using TV model optimization. With TV correction, the estimation quality in smooth regions improves greatly, and the accuracy in occlusion regions can be maintained.

Compared with the deep learning-based disparity estimation, the proposed matching entropy method is applicable for all kinds of light field data and is not affected by the acquisition method and scenario type, while the deep learning-based method relies on the training data set and the applicable scenarios are limited. Especially for the light field data of the actual scene with the diversity of acquisition methods and the actual factors, the advantages of deep learning-based methods cannot be realized. On the other hand, the deep learning-based method usually integrates

the data processing of the light field (such as super-resolution, denoising) into the disparity estimation network, while the proposed matching entropy method directly processes the original light field data to generate the disparity estimation result.

The disadvantage of the the proposed matching entropy is that the scene segmentation is an important premise for our adaptive region identification method. It can be very difficult to obtain accurate segmentation results if the scene is complex. Therefore, we will try to establish a region identification method without segmentation in future work.

7. Conclusion

To accurately estimate depth information from light field data, we propose an adaptive region matching method to match sub-aperture images. Our main contributions are introducing the concept of matching entropy to measure the amount of correct matching information and designing a two-step adaptive process to select optimal matching windows in different regions. From the synthetic and real experiments, we verify that the proposed method can achieve high-precision depth estimation of light field data, especially in occlusion and smooth regions, and is robust to noise. The core idea of defining matching entropy and selecting optimal matching windows adaptively is to treat regions differently according to their characteristics. This idea is not limited to light field data and can also be applied to area matching in more general stereo matching problems.

Disclosures. The authors declare no conflicts of interest.

Data availability. Data underlying the results presented in this paper are not publicly available at this time but may be obtained from the authors upon reasonable request.

References

1. M. Levoy and P. Hanrahan, "Light field rendering," in *Proceedings of the 23rd annual conference on Computer graphics and interactive techniques*, (1996), pp. 31–42.
2. L. Mcmillan and G. Bishop, "Plenoptic modeling: An image-based rendering system," in *Proceedings of the 22nd annual conference on Computer graphics and interactive techniques*, (1995).
3. H. Arimoto and B. Javidi, "Integral three-dimensional imaging with digital reconstruction," *Opt. Lett.* **26**, 157 (2001).
4. X. Xiao, B. Javidi, M. Martinez-Corral, and A. Stern, "Advances in three-dimensional integral imaging: sensing, display, and applications [invited]," *Appl. Opt.* **52**, 546-60 (2013).
5. E. H. Adelson and J. R. Bergen, "The plenoptic function and the elements of early vision," in *Computational Models of Visual Processing*, (MIT Press, 1991), pp. 3-20.
6. R. Ng, M. Levoy, M. Br, G. Duval, M. Horowitz, P. Hanrahan, and D. Design, "Light field photography with a hand-held plenoptic camera," (2005).
7. J. Navarro and A. Buades, "Reliable light field multiwindow disparity estimation," in *2016 IEEE International Conference on Image Processing (ICIP)*, (2016).
8. H. G. Jeon, J. Park, G. Choe, J. Park, Y. Bok, Y. W. Tai, and I. S. Kweon, "Accurate depth map estimation from a lenslet light field camera," in *Computer Vision and Pattern Recognition*, (2015), pp. 1547-1555.
9. C. Chen, H. Lin, Z. Yu, S. B. Kang, and J. Yu, "Light field stereo matching using bilateral statistics of surface cameras," in *Computer Vision & Pattern Recognition*, (2014).
10. K. Mishiba, "Fast depth estimation for light field cameras," *IEEE Transactions on Image Process.* **29**, 1–1 (2020).
11. S. Heber and T. Pock, "Shape from light field meets robust pca," in *European Conference on Computer Vision*, (2014).
12. S. Heber, R. Ranftl, and T. Pock, "Variational shape from light field," in *International Workshop on Energy Minimization Methods in Computer Vision and Pattern Recognition*, (2013).
13. G. P. Fickel, C. R. Jung, T. Malzbender, R. Samadani, and B. Culbertson, "Stereo matching and view interpolation based on image domain triangulation," *IEEE Transactions on Image Process.* **22**, 3353–3365 (2013).
14. S. Wanner, C. Straehle, and B. Goldluecke, "Globally consistent multi-label assignment on the ray space of 4d light fields," in *Computer Vision and Pattern Recognition*, (2013).
15. J. Li, M. Lu, and Z. N. Li, "Continuous depth map reconstruction from light fields," *IEEE Transactions on Image Process.* **24**, 3257–3265 (2015).
16. O. Johannsen, A. Sulc, and B. Goldluecke, "What sparse light field coding reveals about scene structure," in *2016 IEEE Conference on Computer Vision and Pattern Recognition (CVPR)*, (2016).
17. S. Wanner and B. Goldluecke, "Globally consistent depth labeling of 4d light fields," in *2012 IEEE Conference on Computer Vision and Pattern Recognition*, (2012), pp. 41–48.

18. M. Tao, S. Hadap, J. Malik, and R. Ramamoorthi, "Depth from combining defocus and correspondence using light-field cameras," in *ICCV*, (2013).
19. W. Williem and I. K. Park, "Robust light field depth estimation for noisy scene with occlusion," in *Computer Vision and Pattern Recognition*, (2016), pp. 4396–4404.
20. T. C. Wang, A. A. Efros, and R. Ramamoorthi, "Occlusion-aware depth estimation using light-field cameras," in *IEEE International Conference on Computer Vision*, (2016).
21. H. Zhu, Q. Wang, and J. Yu, "Occlusion-model guided antioclusion depth estimation in light field," *IEEE J. Sel. Top. Signal Process.* **11**, 965–978 (2017).
22. Jeon, Hae-Gon, Park, Jaesik, Choe, Gyeongmin, Jinsun, Bok, Yunsu, and T. and, "Depth from a light field image with learning-based matching costs," *IEEE Transactions on Pattern Analysis Mach. Intell.* **41**, 297–310 (2019).
23. C. Shin, H.-G. Jeon, Y. Yoon, I. S. Kweon, and S. J. Kim, "Epinet: A fully-convolutional neural network using epipolar geometry for depth from light field images," in *Proceedings of the IEEE Conference on Computer Vision and Pattern Recognition (CVPR)*, (2018).
24. W. Luo, A. G. Schwing, and R. Urtasun, "Efficient deep learning for stereo matching," in *2016 IEEE Conference on Computer Vision and Pattern Recognition (CVPR)*, (2016), pp. 5695–5703.
25. Y. J. Tsai, Y. L. Liu, M. Ouhyoung, and Y. Y. Chuang, "Attention-based view selection networks for light-field disparity estimation," *Proc. AAAI Conf. on Artif. Intell.* **34**, 12095–12103 (2020).
26. V. Kolmogorov and R. Zabih, "Multi-camera scene reconstruction via graph cuts," in *European Conference on Computer Vision*, (2002).
27. Q. Yang, "Hardware-efficient bilateral filtering for stereo matching," *IEEE Transactions on Pattern Analysis Mach. Intell.* **36**, 1026–32 (2014).
28. A. Buades and G. Facciolo, "Reliable multiscale and multiwindow stereo matching," *Siam J. on Imaging Sci.* **8**, 888–915 (2015).
29. K. Zhang, J. Lu, and G. Lafruit, "Cross-based local stereo matching using orthogonal integral images," *IEEE Transactions on Circuits Syst. for Video Technol.* **19**, 1073–1079 (2009).
30. R. Zabih and J. Woodfill, "Non-parametric local transforms for computing visual correspondence," in *Computer Vision — ECCV '94*, J.-O. Eklundh, ed. (Springer Berlin Heidelberg, Berlin, Heidelberg, 1994), pp. 151–158.
31. I. K. Park, K. M. Lee *et al.*, "Robust light field depth estimation using occlusion-noise aware data costs," *IEEE transactions on pattern analysis machine intelligence* **40**, 2484–2497 (2017).
32. Y. Wang, L. Wang, G. Wu, J. Yang, W. An, J. Yu, and Y. Guo, "Disentangling light fields for super-resolution and disparity estimation," *IEEE Transactions on Pattern Analysis Mach. Intell.* (2022).
33. A. Levin, D. Lischinski, and Y. Weiss, "A closed-form solution to natural image matting," *IEEE Transactions on Pattern Analysis Mach. Intell.* **30**, 228–242 (2008).
34. H. Zhu, Q. Wang, and J. Yu, "Occlusion-model guided antioclusion depth estimation in light field," *IEEE-INST ELECTRICAL ELECTRONICS ENGINEERS INC* (2017).
35. L. I. Rudin, S. Osher, and E. Fatemi, "Nonlinear total variation based noise removal algorithms," *Phys. D Nonlinear Phenom.* **60**, 259–268 (1992).
36. O. Johannsen, K. Honauer, B. Goldluecke, A. Alperovich, F. Battisti, Y. Bok, M. Brizzi, M. Carli, G. Choe, M. Diebold, M. Gutsche, H. Jeon, I. S. Kweon, J. Park, J. Park, H. Schilling, H. Sheng, L. Si, M. Strecke, A. Sulc, Y. Tai, Q. Wang, T. Wang, S. Wanner, Z. Xiong, J. Yu, S. Zhang, and H. Zhu, "A taxonomy and evaluation of dense light field depth estimation algorithms," in *2017 IEEE Conference on Computer Vision and Pattern Recognition Workshops (CVPRW)*, (2017), pp. 1795–1812.